Highly Efficient Sum-Frequency Generation in Niobium Oxydichloride NbOCl$_2$ Nanosheets

Ibrahim Abdelwahab, Benjamin Tilmann, Xiaoxu Zhao, Ivan Verzhbitskiy, Rodrigo Berté, Goki Eda, William L. Wilson, Gustavo Grinblat, Leonardo de S. Menezes, Kian Ping Loh,* and Stefan A. Maier*

Parametric infrared (IR) upconversion is a process in which low-frequency IR photons are upconverted into high-frequency ultraviolet/visible photons through a nonlinear optical process. It is of paramount importance for a wide range of security, material science, and healthcare applications. However, in general, the efficiencies of upconversion processes are typically extremely low for nanometer-scale materials due to the short penetration depth of the excitation fields. Here, parametric IR upconversion processes, including frequency doubling and sum-frequency generation, are studied in layered van der Waals NbOCl$_2$. An upconversion efficiency of up to 0.004% is attained for the NbOCl$_2$ nanosheets, orders of magnitude higher than previously reported values for nonlinear layered materials. The upconverted signal is sensitive to layer numbers, crystal orientation, excitation wavelength, and temperature, and it can be utilized as an optical cross-correlator for ultrashort pulse characterization.

1. Introduction

Direct detection and imaging of infrared (IR) photons demand complex cryogenic apparatus with low sensitivity and high noise.[1] An alternative approach that can address the limitations of IR detectors is to upconvert the IR photons into the ultraviolet (UV)/visible (vis) domain, where room temperature-operating photon detectors are far more efficient.[2] The generation of high-frequency light quanta is also of great interest for a variety of applications such as coherent light sources,[3] photo-therapy,[4] time-domain fluorescence spectroscopy,[5] and nanolithography.[6] Frequency upconversion through a nonlinear parametric sum frequency generation (SFG) has been widely utilized to upconvert IR and vis light into blue and UV light.[7] SFG is a three-wave mixing process in which two incident photons of frequencies ω_1 and ω_2 are converted into an SFG photon at their sum frequency ω_3 ($\omega_3 = \omega_1 + \omega_2$).[8] A special case of SFG is the second-harmonic generation (SHG), which involves two input photons of equal frequencies and one output SHG photon at the doubled frequency ($\omega_1 = \omega_2 = \omega$,

I. Abdelwahab, B. Tilmann, R. Berté, L. de S. Menezes, S. A. Maier
Chair in Hybrid Nanosystems
Nanoinstitute Munich
Faculty of Physics
Ludwig-Maximilians-Universität München
80539, Munich, Bavaria, Germany

I. Abdelwahab, W. L. Wilson
Center for Nanoscale Systems
Harvard University
Cambridge, MA 02138, USA

X. Zhao
School of Materials Science and Engineering
Nanyang Technological University
Singapore 639798, Singapore

I. Verzhbitskiy, G. Eda
Department of Physics and Centre for Advanced 2D Materials
and Graphene Research Centre
National University of Singapore
Singapore 119077, Singapore

R. Berté
Instituto de Física
Universidade Federal de Goiás
Goiânia-GO 74001–970, Brazil

G. Grinblat
Departamento de Física
FCEN
IFIBA-CONICET
Universidad de Buenos Aires
Buenos Aires C1428EGA, Argentina

L. de S. Menezes
Departamento de Física
Universidade Federal de Pernambuco
Recife-PE 50670–901, Brazil

K. P. Loh
Department of Applied Physics
The Hong Kong Polytechnic University
Hung Hom, Kowloon, Hong Kong SAR HKG, P. R. China
E-mail: kploh@polyu.edu.hk

S. A. Maier
Department of Physics
Imperial College London
London SW7 2AZ, UK

S. A. Maier
School of Physics and Astronomy
Monash University
Clayton, Victoria 3800, Australia
E-mail: stefan.maier@monash.edu

**ADVANCED
SCIENCE NEWS**

www.advancedsciencenews.com

**ADVANCED
OPTICAL
MATERIALS**

www.advopticalmat.de

$\omega_3 = 2\omega$). Over several upconversion mechanisms (e.g., energy transfer upconversion, excited-state absorption, photon avalanche, triplet-triplet annihilation, and cooperative energy pooling),[9] SFG is at an advantage since it does not involve the absorption of the input photons by the material, occurs instantaneously, and preserves the coherence of the laser light.

While efficient SFG responses can be achieved in bulk nonlinear crystals through the use of intense pulsed laser beams and careful alignment to fulfill phase matching between the propagating fields,[7] obtaining high SFG upconversion efficiency at the nanoscale remains a challenge. This is due to the weak photon–photon interactions within the limited interaction length in nanometer-scale materials. Resonant nonlinear nanomaterials, including nanoantennas,[10] metasurfaces,[11] and excitonic semiconductors,[12] have been introduced to boost the photon-to-photon upconversion efficiency at subwavelength interaction lengths. However, resonances come at the cost of optical losses due to absorption.

Relying on the fact that the second-order nonlinear SFG process occurs only in noncentrosymmetric materials (in the electric dipole approximation), ferroelectrics[13] possess broken inversion symmetry, which makes them strong candidates for achieving parametric upconversion. Layered ferroelectric transition metal oxidehalides exhibit very large spontaneous polarization due to their polar Peierls-distorted structure.[14] Niobium oxide dihalides $NbOX_2$ (X = Cl, Br, I) are archetypical examples of this class of layered materials. $NbOX_2$ exhibits high thermodynamic stability and nearly thickness-independent band structure.[15] When the light-induced nonlinear polarization is coupled with the spontaneous polarization of $NbOX_2$, large second-order optical nonlinearities can be attained, which can then be exploited in the high-efficient generation of light associated with such second-order processes like SHG and SFG.[15a] In this work, we first study the SHG response of exfoliated $NbOCl_2$ nanosheets under femtosecond (fs) near-IR laser pumping. We find that $NbOCl_2$ nanosheets exhibit a very intense SHG (i.e., frequency doubling) that varies with the excitation wavelength and pump laser polarization, besides increasing with the material thickness, that is, the number of stacked nanosheets, up to the thickest samples we investigated. Within the investigated pumping wavelength range and excitation powers, no third-harmonic generation (THG) could be detected. However, the spectral region around that of THG could be filled through a highly efficient SFG between the near-IR pump pulses and their frequency-doubled replica, which populates more densely the spectral range in which upconversion can be observed. Lastly, we employed the time-resolved SFG signal within the thin $NbOCl_2$ sheet to demonstrate the potential of this novel material as a nanosized intensity cross-correlator for measuring ultrashort pulse durations, which meets the requirements for building highly efficient, flat optics devices demanded by modern nanophotonics approaches.

2. Results and Discussion

Centimeter-sized $NbOCl_2$ single crystals were grown by chemical vapor transport (see Experimental Section for growth specifics). In order to get a complete image of the structural details of $NbOCl_2$, we performed single-crystal X-ray diffraction (SC-XRD) and scanning transmission electron microscopy (STEM) measurements. **Figure 1**a and Figure S1, Supporting Information, schematize the sheet structure of $NbOCl_2$. $NbOCl_2$ crystallizes in the noncentrosymmetric space group C2 (No. 5) as confirmed by SC-XRD analysis (refer to Table S1, Supporting Information, and supplementary crystallographic information files [CIFs] for the crystallographic data). Each Nb atom is surrounded by 4 Cl and 2 O atoms in a trans configuration forming a distorted octahedron. The NbO_2Cl_4 octahedra share Cl–Cl edges (in the c direction) and O corners (in the b direction) with four other octahedra to form sheets parallel to the (100) crystallographic plane. The thickness of the $NbOCl_2$ monolayer is ≈0.64 nm. The Nb atoms are displaced from the centers of the octahedra in the c direction, thus forming Nb–Nb pairs. The alternatingly short and long Nb–Nb distances are 2.96 and 3.90 Å, respectively. The Nb atoms are also displaced from the mirror planes (i.e., the planes of the surrounding four Cl atoms) of the octahedra by ≈0.17 Å, giving rise to two Nb–O bonds of unequal lengths. The alternatingly short and long Nb–O bond lengths are 1.78 and 2.13 Å, respectively. Since all Nb_2 pairs are shifted in the same direction out of the mirror planes, the crystal exhibits polarity along the b-axis. The metal–metal bonding (i.e., Nb_2 pairs) represents a first-order Peierls distortion, while the formation of unequal Nb–O bonds can be interpreted as a second-order Peierls distortion.[16]

The weak van der Waals (vdW) forces between the adjacent sheets allow easy cleavage of the bulk $NbOCl_2$ crystals into nanosheets. Figure 1b shows atomically resolved STEM images of $NbOCl_2$ nanosheet projected at the [100] zone axis (i.e., layer-stacking a direction). The atomic arrangement of the sample is in line with the SC-XRD model as shown in Figure 1b right panel. The STEM diffraction analysis of the sample is shown in Figure 1c. The appearance of superspots in the experimental 2D electron diffraction pattern confirms the periodic lattice modulations (i.e., Peierls distortions). It matches the simulated electron diffraction pattern generated by the theoretical modeling of the $NbOCl_2$ lattice. Nonetheless, the periodic modulations cannot be seen in the STEM images at a perfect zone axis due to the staggered AA packing structure of $NbOCl_2$ (β = 105.5°, and each layer is shifted by 6.7 Å relative to the layer below in the direction parallel to the c axis). The projected Nb atom displacements thereupon cancel each other in thick flakes. The Nb displacements can only be seen when the sample surface is tilted away from the [100] zone axis. Figure 1d depicts the periodic distortion of the Nb dimers acquired along the [001] zone axis.

Figure 2a displays the calculated density functional theory (DFT) energy band structure and projected density of states (PDOS) for the $NbOCl_2$ monolayer.[17] The results indicate that the $NbOCl_2$ monolayer is an indirect gap semiconductor with a bandgap of 0.82 eV. The DFT method provides a qualitative description of the band structure but should not be used for quantitative analysis as it substantially underestimates the fundamental gap (by >1 eV for $NbOX_2$).[15a] The highest valence bands arise primarily from Cl p and O p orbitals except for the band edge (the red line in the proximity of the Fermi level), which originates from localized Nb $d_{x^2-y^2}$/Nb d_{z^2} mixed states. The lowest conduction bands
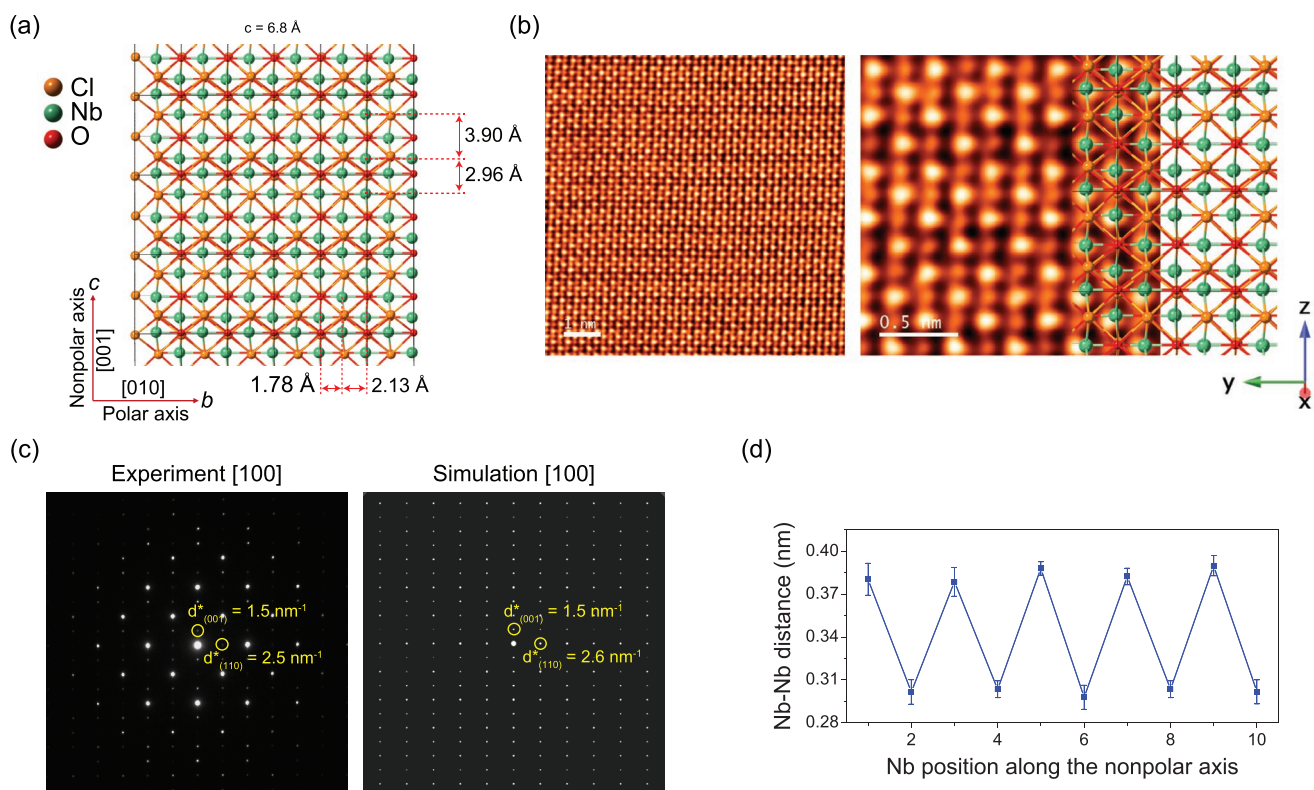
Figure 1. a) Schematic representation of the sheet structure of bilayer $NbOCl_2$ as determined by SC-XRD. b) Atomic-resolution STEM-ADF images of $NbOCl_2$ flake taken in the [100] direction at different magnifications. The atomic model is overlaid on the high-magnification STEM image to highlight the positions of the different atomic constituents of $NbOCl_2$. c) Experimental and simulated electron diffraction patterns in $NbOCl_2$ along the [100] zone axis. d) Nb-Nb periodic lattice modulation acquired along the [001] zone axis of $NbOCl_2$.

are mainly attributed to Nb d orbitals. The Peierls distortions split the bands in the vicinity of the Fermi level, which lowers the electron energy of the highest occupied states. The effective overlap between the Nb d orbitals and the O p orbitals triggers highly dispersive low-lying conduction bands along the polar axis (Γ–Y). On the contrary, the conduction bands are weakly dispersive along the nonpolar axis (Γ–X). The anisotropic dispersion of the $NbOCl_2$ band structure brings about strongly direction-dependent optical properties. Figure 2b shows the absorption spectra of $NbOCl_2$ along the polar and nonpolar axes in the vis range. The optical absorption is excitonic in nature and is more efficient along the nonpolar axis than the polar axis, especially in the blue range. The optical anisotropy is also reflected in the transmission optical images of the $NbOCl_2$ nanosheet collected with incident white light polarized along the nonpolar (Figure 2c) and polar (Figure 2d) axes. The excitonic absorption of $NbOCl_2$ in the vis range is not as strong as that of $NbOI_2$ due to the large optical bandgap of $NbOCl_2$.[15a] Furthermore, the strong in-plane anisotropy of $NbOCl_2$ is manifested in its mechanical properties (Young's moduli along the polar and nonpolar axes are 92.9 and 62 m N^{-1}, respectively),[14] leading typically to rectangular $NbOCl_2$ flakes preferentially cleaved along their nonpolar axis. This means that the crystal orientation of the $NbOCl_2$ nanosheets can be identified by simply observing their morphology using optical microscopy.

To evaluate the performance of air-stable $NbOCl_2$ nanosheets exfoliated on a quartz substrate (**Figure 3**a) as parametric IR upconverters, we first study their SHG response with near-IR laser pulses (for details see Experimental Section, Nonlinear Optical Characterization) propagating normal to the surface of the sheets. Figure 3b,c depicts representative 2D SHG intensity maps of the same area region as seen in the optical microscopy image shown in Figure 3a when excited at $\lambda_{pump} = 900$ nm ($\lambda_{SHG} = 450$ nm) along the polar and nonpolar axes, respectively. We find that the emitted SHG signal is strongest when the excitation field is aligned along the polar axis of $NbOCl_2$. This is also reflected in the SHG polar plot of $NbOCl_2$ (Figure 3d) in which the total SHG intensity is measured as a function of the excitation polarization angle. The dumbbell-shaped angular SHG intensity pattern is anticipated from the 1D ferroelectric nature of $NbOCl_2$, which induces a large SHG tensor element (d_{22}) around the polar axis.[15a] The polarization of the detected SHG light parallel (Y) and perpendicular (Z) to the polar axis is also analyzed and found to be strongly polarized along the polar direction (Figure S2, Supporting Information). The refractive indices along the polar axis of $NbOCl_2$ are 1.68 and 1.88 at the fundamental (900 nm) and SH (450 nm) wavelengths, respectively, and thus, the measured SHG of $NbOCl_2$ is considered a non-phase-matched nonlinear signal. In Figure 3e and Figure S3, Supporting Information, the SHG response is measured with varying excitation laser wavelength
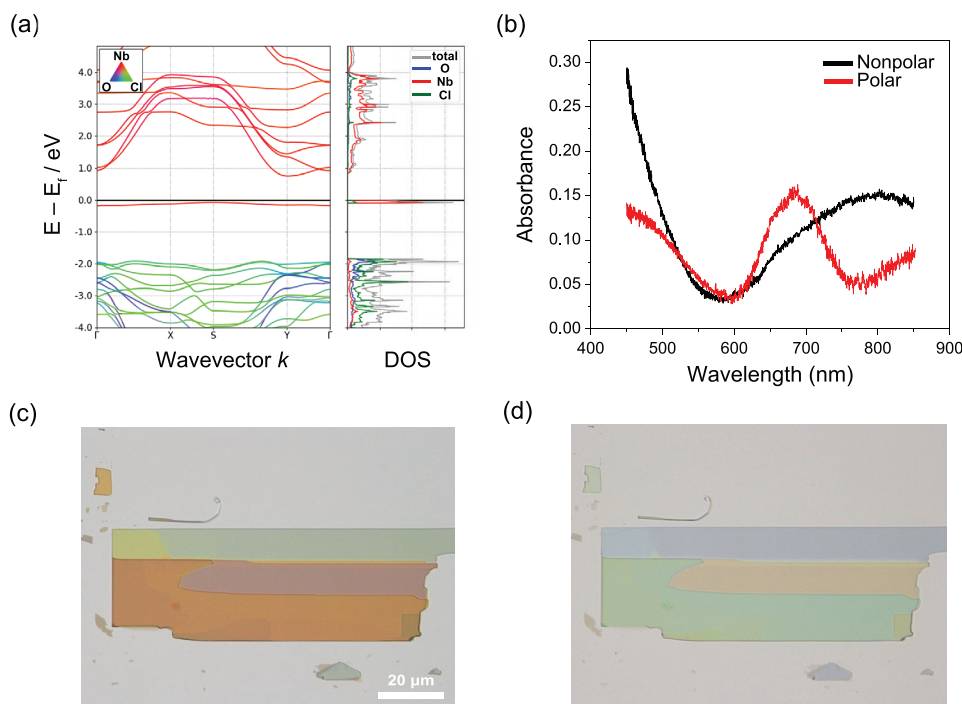
Figure 2. a) DFT calculated energy band structure and projected density of states (DOS) of $NbOCl_2$ monolayer. The $\Gamma \rightarrow Y$ and $\Gamma \rightarrow X$ high-symmetry directions in the reciprocal space (k-space) correspond respectively to the polar (Nb—O⋯Nb) and nonpolar (Nb—Nb⋯Nb) directions of $NbOCl_2$ in real space. The valence band maximum is set to zero energy. b) Linear absorbance spectra of $NbOCl_2$ nanosheet collected with incident white light polarized along the polar and nonpolar directions. Black (red) line: nonpolar (polar) axis. c,d) Optical images of a $NbOCl_2$ flake captured in a transmitted light mode with incident white light polarized along the nonpolar (c) and polar (d) directions. Scale bar, 20 µm.

(λ_{pump} = 850–1600 nm). While SHG light tuneable across the entire vis spectrum is attained, the response is largest in the blue spectral region. It indicates that the SHG signal is resonantly enhanced at the high-frequency excitonic states of $NbOCl_2$. The thickness-dependent intensity variation of the reflected SHG signal of $NbOCl_2$ (Figure 3f) is attributed to the interference effects between the surface and bulk SHG contributions, which result in oscillations in the overall SHG signal.[18]

The SHG intensity at λ_{SHG} = 450 nm is plotted as a function of excitation power in Figure 3g. The log scale plot (Figure 3h) shows a linear dependence with a slope equal to 1.99, demonstrating that the expected quadratic power dependence of the SHG signal on the excitation power is held up to 150 µW average power (4.2 kW peak power). The IR upconversion efficiency (η) (that is the parameter that determines whether the nonlinear material satisfies the performance requirements for real applications) is measured by dividing the SHG output power in watts by the input power in watts and is expressed as a percentage. Remarkably, a maximum η_{SHG} of 0.002% is attained for the $NbOCl_2$ nanosheets in a reflection mode and within the studied samples' thickness range (≤120 nm), indicating a total η_{SHG} of at least 0.004% when considering the radiation emitted in the upper half of the microscope and not collected by the objective, which is orders of magnitude higher than values reported for other nonlinear 2D materials.[15] For example, the reported η_{SHG} for GaTe nanosheet is 1.8×10^{-8}% and for GaSe nanosheet is 6.1×10^{-7}% at λ_{SHG} = 780 nm.[19]

The forward (transmitted) radiated SHG output power was also measured and found to be very much comparable to the backward (reflected) SHG power. The total sheet second-order susceptibility $\chi^{(2)}_{s,SHG}$ can be expressed in terms of the fundamental and SHG powers as follows[20]

$$\chi^{(2)}_{s,SHG} = \sqrt{\frac{\varepsilon_o c \lambda^4_{SHG} P_{SHG} R \tau^2_{Pump} (n_{SHG}+1)^2 (n_{Pump}+1)^4}{32 NA^2 \tau_{SHG} P^2_{Pump} \phi}} \quad (1)$$

where ε_o is the vacuum permittivity, c is the speed of light in vacuum, λ_{SHG} is the SHG wavelength, P is the average power, R is the laser repetition rate, τ is the pulse width, n_{Pump} and n_{SHG} are the refractive indices of the substrate (quartz) at the fundamental and SHG wavelengths, NA is the numerical aperture of the objective lens, and ϕ is the solid angle of the scattered beam. We obtained $\chi^{(2)}_{s,SHG}$ of $\approx 1.9 \times 10^{-18}$ m V^{-1}, which is equivalent to an effective bulk-like second-order susceptibility $\chi^{(2)}_{eff,SHG}$ of $\approx 4.9 \times 10^{-11}$ m V^{-1} ($\chi^{(2)}_{eff} = \frac{\chi^{(2)}_s}{t}$, where t = 38 nm is the thickness of the $NbOCl_2$ sheet). This is more than an order of magnitude higher than $\chi^{(2)}_{SHG}$ of conventional nonlinear crystals such as beta-barium borate (β-BaB$_2$O$_4$ or BBO) crystal (d_{22} = 0.23 (0.20) $\times 10^{-11}$ m V^{-1} at λ_{pump} = 852 (820) nm).[21a,b] Up to the maximum laser power used, no THG signal ($\omega_3 = \omega + \omega + \omega$) was observed, suggesting that $NbOCl_2$ has a negligible third-order susceptibility $\chi^{(3)}$ within the wavelength range and excitation conditions of this study.

We now turn to the three-wave mixing of three different frequencies. In principle, one can mix the pump beam at ω_1
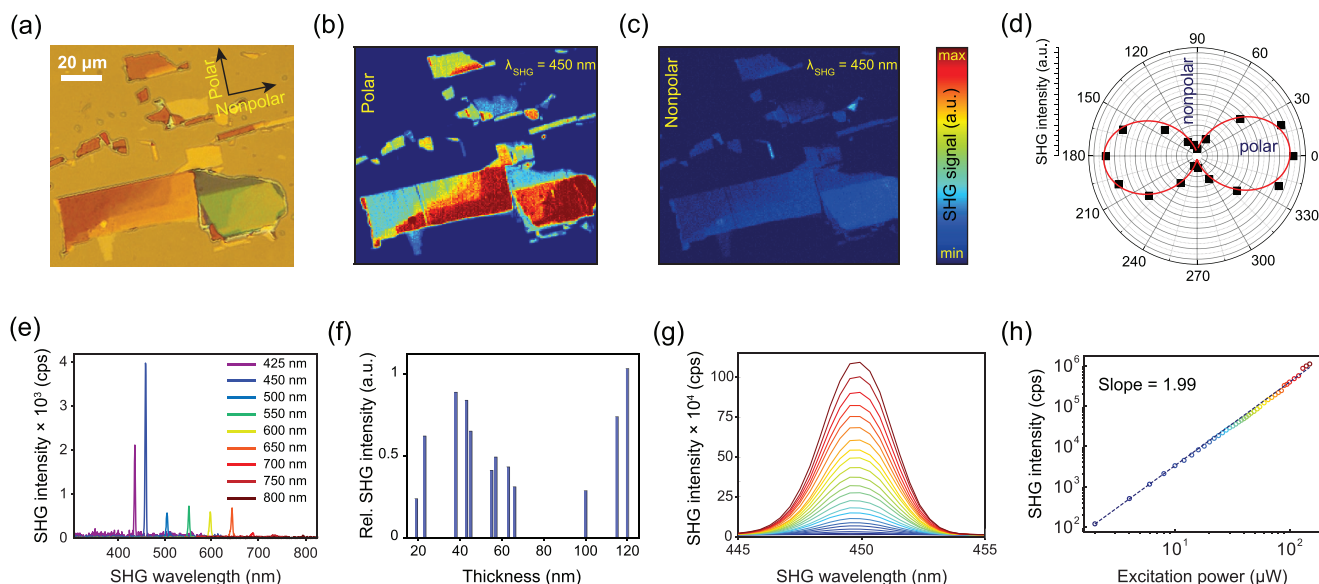
Figure 3. a) Optical microscope image of NbOCl$_2$ flakes on a quartz substrate. b,c) SHG intensity maps recorded with an avalanche photodiode (APD) of the sample shown in a) at $\lambda_{SHG} = 450$ nm obtained by setting the excitation polarization parallel to the polar (b) and nonpolar (c) directions of NbOCl$_2$ while maintaining constant excitation intensities. d) Polar plot of the total SHG intensity as a function of the polarization angle of the excitation beam at $\lambda_{SHG} = 450$ nm. The black dots represent the experimental data while the solid red line represents the theoretical fit (considering the Kleinman symmetry). e) The intensity dependence of SHG on the fundamental wavelength demonstrated by SHG spectra at $\lambda_{pump} = 850, 900, 1000, 1100, 1200, 1300, 1400, 1500,$ and 1600 nm. The sample is excited by equally intense excitation pulses linearly polarized along the polar axis. The enhancement of the SHG signal in the blue spectral region is attributed to the combined effect of ferroelectricity and two-photon resonance at the NbOCl$_2$ exciton states. f) The intensity dependence of SHG on the layer thickness at $\lambda_{SHG} = 450$ nm. g) Excitation power dependence of the SHG spectrum peaking at $\lambda_{SHG} = 450$ nm in the excitation power range of 2 (lower, blue curve) to 150 μW (upper, wine curve). h) The log–log scaled SHG intensity versus excitation power plot. The slope of the linear fit is equal to 1.99, confirming the second-order nature of the generated nonlinear signal.

with the SHG beam at ω_2 within NbOCl$_2$ to generate an SFG signal at ω_3 ($\omega_3 = \omega + 2\omega$). In this regard, we mixed two pumps (Y-polarized, $\lambda_1 = 1200$ nm and $\lambda_2 = 600$ nm) spatiotemporally overlapped from which a strong SFG signal was observed at $\lambda_{SFG} = 400$ nm (wavelength at which the sensitivity of our detection setup is close to its minimum) (**Figure 4**a). To confirm the nature of this specific nonlinear process, the SFG signal intensity is measured as a function of the pump power by fixing the power of one beam while gradually varying the power of the other one. Each excitation beam contributes one photon to the SFG process, resulting in a linear power dependence for both experiments considered here. As shown in Figure 4b,c, slopes of 0.99 and 1.07 are obtained by fitting in bilogarithmic plots, which are close to the theoretical value 1 of the typical log–log curve for SFG processes.[8] To estimate the SFG upconversion efficiency, we mapped both SFG and SHG signals as a function of the spatial position of the NbOCl$_2$ flake at similar pump powers (i.e., the pump power for SHG is equal to the square root of the product of the pump powers for SFG), shown in Figures 4d and 4e, respectively. After taking into account the different transmission values at 400 and 600 nm of the beam splitter used in our microscope, as well as the detection efficiencies at these wavelengths of the APD used for taking the data shown in Figure 4d,e, we got a spectral intensity of SFG which is ≈98% of the SHG intensity. This means that by detuning the excitation beams to $\lambda_1 = 900$ nm and $\lambda_2 = 450$ nm, a highly efficient UV SFG signal at 300 nm with a maximum η_{SFG} of 0.004% could realistically be achieved. This is an order

of magnitude higher than the reported η_{SFG} for AlGaAs nanoantennas.[10] For two different excitation frequencies (ω_1, ω_2), Equation (1) can be rewritten as

$$\chi^{(2)}_{s,SFG} = \sqrt{\frac{\varepsilon_o c \lambda_{SFG}^4 P_{SFG} R \tau_{\omega_1} \tau_{\omega_2} (n_{SFG} + 1)^2 (n_{\omega_1} + 1)^2 (n_{\omega_2} + 1)^2}{32 N A^2 \tau_{SFG} P_{\omega_1} P_{\omega_2} \phi}} \quad (2)$$

We obtained $\chi^{(2)}_{s,SFG}$ of ≈5.1 × 10^{-19} m V^{-1} and $\chi^{(2)}_{eff,SFG}$ of ≈1.4 × 10^{-11} m V^{-1}.

The second-order nonlinear conversion efficiency is also found to increase sevenfold by reducing the temperature to 78 K (Figure S4, Supporting Information) due to enhanced spontaneous polarization and excitonic effects. The AA-stacked NbOCl$_2$ crystal has a broken inversion symmetry regardless of thickness and its nonlinear $\chi^{(2)}_s$ and η scale with thickness, whereas many nonlinear 2D materials (e.g., MoS$_2$ and SnS) exhibit an odd-even layer-number effect that leads to the cancellation of the net dipole moment in bulk form, constraining the nonlinear response to atomically thin sheets.[22] The high upconversion efficiency of SFG makes NbOCl$_2$ amenable to enhancing second-order processes other than SFG, finding applications such as its use as a frequency-converting material in optical parametric oscillators and spontaneous parametric downconversion for the generation of squeezed coherent states and entangled states of light.[23] It paves the way for on-chip classical and quantum photonic regimes of relaxed phase matching.

SFG is very sensitive to the temporal overlap of the two excitation pulses, and therefore, it can be utilized for
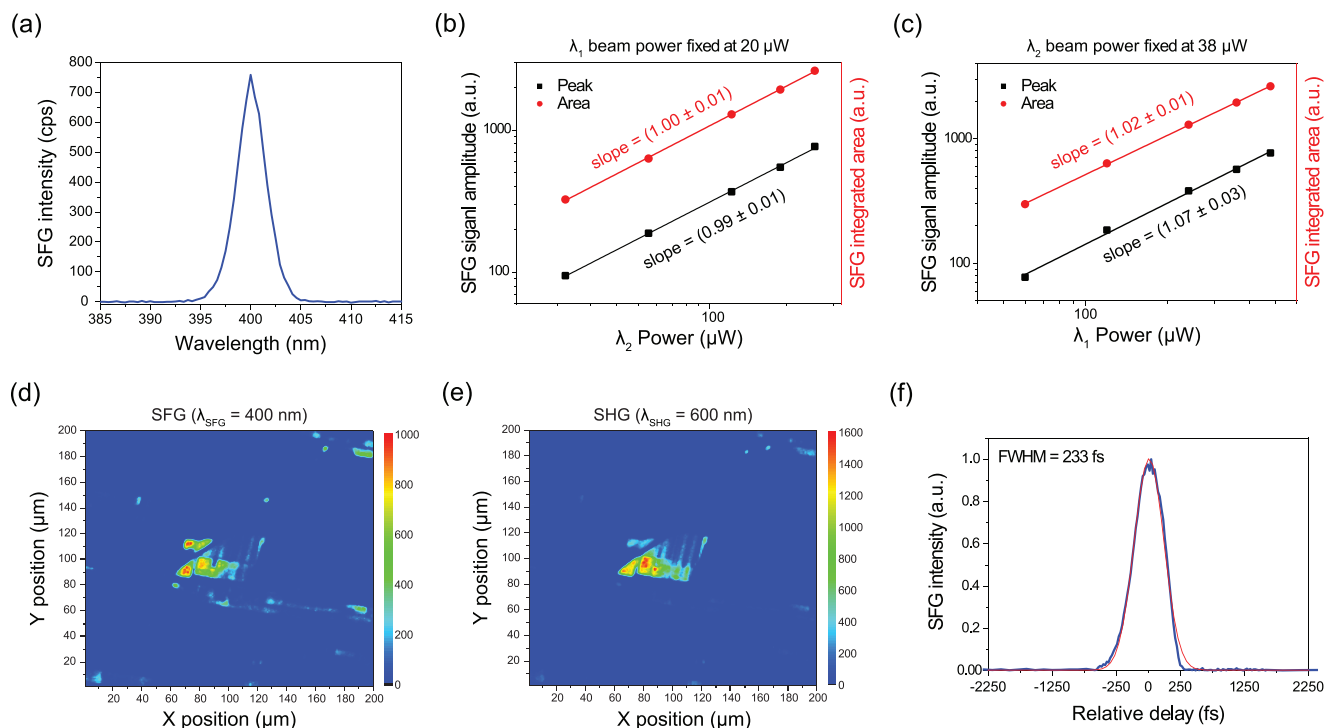
Figure 4. a) SFG spectrum at λ_{SFG} = 400 nm after mixing λ_1 = 1200 nm and λ_2 = 600 nm pump pulses. b) Dependence of the SFG intensity on the λ_2 pump power while fixing the power of the beam at λ_1. c) SFG intensity measured by varying the power of the beam at λ_1 power while keeping the power of the beam at λ_2 constant. Solid lines are linear power fits on a log–log scale with slopes around 1, confirming the expected linear dependence of the SFG intensity on the power of each mixing beam individually. In b,c) the results are shown considering the peak value (black squares) and the integrated area (red circles) under the SFG spectrum, respectively. d,e) SFG and SHG intensity maps (non-corrected for microscope beam splitter transmissions and APD detection efficiencies at 400 and 600 nm) recorded at similar pump powers (i.e., the pump power for SHG is equal to the square root of the product of the pump powers for SFG). The pump wavelengths are λ_1 = 1200 nm and λ_2 = 600 nm for SFG and λ_1 = 1200 nm for SHG. f) Time-resolved SFG intensity profile (in blue) and sech²-fitting curve (in red) plotted as a function of the λ_1 delay time. It is recorded by temporally scanning the λ_1 pulses across the λ_2 pulses within the NbOCl₂ nanosheet. The pumps have polarization parallel to the polar axis of NbOCl₂ for all the SFG measurements.

characterizing unknown ultrafast laser pulses through intensity auto- (in case of SHG) and cross-correlation (in case of SFG) measurements.[24] In that context, the power of the SFG signal is recorded as a function of the relative time delay between the pulses of the beams at the wavelengths λ_1 and λ_2. Figure 4f represents the temporal profile of the SFG response created by temporally scanning the laser pulses at λ_1 = 1200 nm across the laser pulses at λ_2 = 600 nm within the NbOCl₂ nanosheet via a variable optical delay line. The pulse duration of the temporal intensity profile of the SFG pulses is ≈233 fs full width at half maximum (FWHM). The dependence of the cross-correlation intensity ($A_{cc}(\tau)$) on the temporal delay is given by

$$A_{cc}(\tau) \propto \int_{-\infty}^{\infty} I_{\lambda_2}(t) I_{\lambda_1}(t-\tau) dt \qquad (3)$$

where $I(t)$ is the temporal intensity profile of the laser pulses. From the measured SFG cross-correlation trace, one can readily retrieve the pulse duration of the test (excitation) pulses if the pulse shape is known. Assuming hyperbolic secant square (sech²) pulse shapes for our two ultrafast pump pulses and considering that the FWHM of the pulses at 600 nm is that of 1200 nm/√2, the pulse duration of the IR laser pulses at 1200 nm was measured to be 190 fs FWHM. This is in very good agreement with the manufacturer's specifications of 180 fs FWHM for our ≈4-year-old laser system.

3. Conclusion

In summary, we investigated the nonlinear optical properties of layered NbOCl₂ using multiphoton nonlinear optical microscopy, where extremely large second-order optical responses (SHG, SFG) are observed in the UV/vis within interaction lengths much shorter than the optical wavelength. The low-temperature measurement shows a sevenfold enhancement of the upconversion process efficiency. The strong nonlinearities are attributed to the large net permanent dipole moment of NbOCl₂ and are boosted by exciton resonances. The upconverted emission intensity varies strongly with the layer thickness, as well as the input polarization and wavelength. The SFG signal is utilized as an optical cross-correlator for determining the duration of ultrashort pulses, for which an electronic device (e.g., a photodiode) would be too slow. The high upconversion efficiency of NbOCl₂ offers the possibility of designing high-performance on-chip nonlinear nanodevices such as tuneable laser sources, ultrathin optical auto- and cross-correlators, and entangled photon pairs generators.

4. Experimental Section

Crystal Growth: NbOCl₂ single crystals were grown by chemical vapor transport. NbOCl₂ crystals were synthesized from high-purity

**ADVANCED
SCIENCE NEWS**

www.advancedsciencenews.com

**ADVANCED
OPTICAL
MATERIALS**

www.advopticalmat.de

Nb metal (film), $NbCl_5$ (powder), and Nb_2O_5 that were mixed to form a stoichiometric ratio Nb:O:Cl = 1:1:2 and sealed in an evacuated (10^{-5} mbar) quartz ampule. Sealed ampules were placed in a horizontal dual-zone furnace and brought to 600 °C at the rate of 1 °C min^{-1}. A chemical transport reaction took place by means of the equilibrium

$$NbOCl_2(s) + NbCl_5(g) \rightleftharpoons NbOCl_3(g) + NbCl_4(g) \tag{4}$$
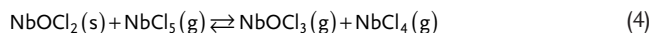
The ampules were held at 600 °C for 5 days, then slowly cooled for 10 days with slightly different rates at the hot (1.2 °C h^{-1}) and cold (1.5 °C h^{-1}) zones. This small temperature gradient ensured the growth of centimeter-size high-quality crystals near the cold end of the ampule. After the slow-cooling process, the furnace was turned off allowing the ampules to cool down naturally. Crystals were extracted from the opened ampules and then stored for future use.

X-ray Crystallographic Analysis: The SC-XRD data were collected at room ($T = 298$ K) and low ($T = 100$ K) temperatures on a Bruker D8 Venture SC-XRD system equipped with Mo Kα radiation ($\lambda = 0.71073$ Å), KAPPA four-circle goniometer, PHOTON 100 detector (CMOS APS), and Oxford Cryostream. Data collection, integration, and scaling were carried out using the Bruker APEX3 software package. The frames were integrated with the Bruker SAINT software package using a narrow-frame algorithm. Data were corrected for absorption effects using the multi-scan method (SADABS). The structures were solved and refined using the Bruker SHELXTL Software Package, using the space group C 1 2 1, with $Z = 4$ for the formula unit, Cl_2NbO. The final anisotropic full-matrix least-squares refinement was carried out on weighted F^2 values. Relevant crystal, collection, and refinement data for the crystal structures of $NbOCl_2$ at 298 and 100 K are summarized in Table S1, Supporting Information.

CCDC 2231643–2231644 contains the supplementary crystallographic data for this paper. These data can be obtained free of charge from The Cambridge Crystallographic Data Centre via www.ccdc.cam.ac.uk/data_request/cif.

STEM Characterization: Atomic-resolution STEM-ADF imaging was performed on an aberration-corrected JEOL ARM200F, equipped with a cold field-emission gun and an ASCOR corrector operating at 80 kV. The convergence semiangle of the probe was around 30 mrad. The collection angle for high-angle annular dark-field imaging was between 81 and 280 mrad and for medium-angle annular dark-field imaging was from 30 to 110 mrad.

Thin Sample Preparation: The bulk $NbOCl_2$ crystals were mechanically exfoliated in the air onto clean quartz substrates (for linear absorption and SHG/SFG characterizations) or TEM grids (for STEM characterization) using the Scotch tape method. Atomic force microscopy (AFM) was used to measure the thickness of the exfoliated flakes.

Micro-Absorption Measurement: The micro-absorption measurement was performed by placing the $NbOCl_2$ sample between aligned microscope objectives (50X Mitutoyo, apochromat, infinity corrected), for light focusing and collection. Pulsed laser (Coherent Libra) with a fundamental wavelength of 800 nm, pulse width of ≈50 fs, and repetition rate of 1 kHz was focused on a sapphire crystal to generate a broadband white light. The light was passed through a 750 nm short-pass filter to eliminate the residual from the fundamental, before collimation using a parabolic mirror. The light was then sent to the objective and focused into a ≈2 µm spot for the absorption measurement. The absorption spectra were obtained by comparing the transmitted light spectra between the samples and a blank (quartz). The spectral detection was done using a monochromator (Princeton Instrument) and a photomultiplier tube setup.

Nonlinear Optical Characterization: For the SHG measurements, a femtosecond pulsed Yb:KGW PHAROS laser system pumping of a collinear optical parametric amplifier ORPHEUS (Light Conversion Ltd, pulse duration of 180 fs, a repetition rate of 200 kHz, tunable output of 210–2200 nm) was used. The excitation beam was focused onto the sample with a 100× (NA = 0.9) air objective from Nikon (≈1 µm^2 spot size). The spectral range of the excitation beam was tuned from 850 to 1600 nm in steps of 50 nm. The nonlinear emission was collected in

a back-scattering configuration via the same objective or in a forward-scattering configuration via another objective and detected with an avalanche photodiode (MPD PDM Series by PicoQuant) for imaging, or by a spectrograph (Acton SP2300 by Princeton Instruments) for spectral measurements. The sample was fixed to an XYZ piezo-scanner stage (Nano-Drive, Mad City Labs) to perform the sample scanning. The excitation and detection polarizations were controlled with half-wave plates, in combination with linear polarizers. The power of the collected SHG emission was measured with a calibrated silicon photodetector (Newport), while the excitation power was characterized with a germanium photodetector (Thorlabs). A continuous-flow optical microscopy cryostat was used for the low-temperature measurements. For SFG, the same laser setup was used in combination with an optical delay line with <1 fs time resolution. The two excitation beams were focused collinearly onto the sample and the temporal delay between them was controlled by the delay line.

Supporting Information

Supporting Information is available from the Wiley Online Library or from the author.

Conflict of Interest

The authors declare no conflict of interest.

Data Availability Statement

The data that support the findings of this study are available in the supplementary material of this article.

ADVANCED
SCIENCE NEWS

www.advancedsciencenews.com

ADVANCED
OPTICAL
MATERIALS

www.advopticalmat.de

[1] A. Rogalski, *Infrared Detectors*, CRC Press, Boca Raton, FL, USA **2000**.

[2] a) C.-M. M. del Rocio, R. Davide, X. Lei, F. G. Valerio, D. Nikolay, S. Lyubomir, M. Zhonghua, K. Andrei, L. Mykhaylo, K. Fouad, A. D. Alexander, H. T. H. Hoe, L. Giuseppe, A. Costantino De, J. Chennupati, E. M. Andrey, R. Mohsen, N. N. Dragomir, *Adv. Photonics* **2021**, *3*, 036002; b) K. Huang, Y. Wang, J. Fang, W. Kang, Y. Sun, Y. Liang, Q. Hao, M. Yan, H. Zeng, *Photonics Res.* **2021**, *9*, 259.

[3] S. V. Makarov, A. N. Tsypkin, T. A. Voytova, V. A. Milichko, I. S. Mukhin, A. V. Yulin, S. E. Putilin, M. A. Baranov, A. E. Krasnok, I. A. Morozov, P. A. Belov, *Nanoscale* **2016**, *8*, 17809.

[4] E. C. Friedberg, *Nature* **2003**, *421*, 436.

[5] J. R. Lakowicz, *Principles of Fluorescence Spectroscopy*, Springer, New York **2006**.

[6] B. Wu, A. Kumar, *J. Vac. Sci. Technol., B: Microelectron. Nanometer Struct. – Process., Meas., Phenom.* **2007**, *25*, 1743.

[7] V. G. Dmitriev, G. G. Gurzadyan, D. N. Nikogosyan, *Handbook of Nonlinear Optical Crystals*, Vol. 64, Springer, New York **2013**.

[8] A. Morita, *Theory of Sum Frequency Generation Spectroscopy*, Vol. 97, Springer, New York **2018**.

[9] a) M. Wu, D. N. Congreve, M. W. B. Wilson, J. Jean, N. Geva, M. Welborn, T. Van Voorhis, V. Bulović, M. G. Bawendi, M. A. Baldo, *Nat. Photonics* **2016**, *10*, 31; b) J. Zhou, Q. Liu, W. Feng, Y. Sun, F. Li, *Chem. Rev.* **2015**, *115*, 395; c) D. H. Weingarten, M. D. LaCount, J. van de Lagemaat, G. Rumbles, M. T. Lusk, S. E. Shaheen, *Nat. Commun.* **2017**, *8*, 14808.

[10] A. Zilli, D. Rocco, M. Finazzi, A. Di Francescantonio, L. Duò, C. Gigli, G. Marino, G. Leo, C. De Angelis, M. Celebrano, *ACS Photonics* **2021**, *8*, 1175.

[11] R. Camacho-Morales, D. Rocco, L. Xu, V. F. Gili, N. Dimitrov, L. Stoyanov, Z. Ma, A. Komar, M. Lysevych, F. F. Karouta, A. Dreischuh, H. H. Tan, G. Leo, C. De Angelis, C. Jagadish, A. E. Miroshnichenko, M. Rahmani, D. N. Neshev, *Adv. Photonics* **2021**, *3*, 036002.

[12] a) Y. Kim, H. Kim, H. Jang, J.-H. Ahn, J. D. Lee, *Nano Lett.* **2020**, *20*, 4530; b) K. Yao, E. Yanev, H.-J. Chuang, M. R. Rosenberger, X. Xu, T. Darlington, K. M. McCreary, A. T. Hanbicki, K. Watanabe, T. Taniguchi, B. T. Jonker, X. Zhu, D. N. Basov, J. C. Hone, P. J. Schuck, *ACS Nano* **2020**, *14*, 708.

[13] C. Cui, F. Xue, W.-J. Hu, L.-J. Li, *npj 2D Mater. Appl.* **2018**, *2*, 18.

[14] Y. Wu, I. Abdelwahab, K. C. Kwon, I. Verzhbitskiy, L. Wang, W. H. Liew, K. Yao, G. Eda, K. P. Loh, L. Shen, S. Y. Quek, *Nat. Commun.* **2022**, *13*, 1884.

[15] a) I. Abdelwahab, B. Tilmann, Y. Wu, D. Giovanni, I. Verzhbitskiy, M. Zhu, R. Berté, F. Xuan, L. d. S. Menezes, G. Eda, T. C. Sum, S. Y. Quek, S. A. Maier, K. P. Loh, *Nat. Photonics* **2022**, *16*, 644; b) Y. Jia, M. Zhao, G. Gou, X. C. Zeng, J. Li, *Nanoscale Horiz.* **2019**, *4*, 1113.

[16] R. E. Peierls, *Quantum Theory of Solids*, Clarendon Press, Oxford, UK **1996**.

[17] J. Zhou, L. Shen, M. D. Costa, K. A. Persson, S. P. Ong, P. Huck, Y. Lu, X. Ma, Y. Chen, H. Tang, Y. P. Feng, *Sci. Data* **2019**, *6*, 86.

[18] S. Deckoff-Jones, J. Zhang, C. E. Petoukhoff, M. K. L. Man, S. Lei, R. Vajtai, P. M. Ajayan, D. Talbayev, J. Madéo, K. M. Dani, *Sci. Rep.* **2016**, *6*, 22620.

[19] a) J. Susoma, L. Karvonen, A. Säynätjoki, S. Mehravar, R. A. Norwood, N. Peyghambarian, K. Kieu, H. Lipsanen, J. Riikonen, **2016**, *108*, 073103; b) L. Karvonen, A. Säynätjoki, S. Mehravar, R. D. Rodriguez, S. Hartmann, D. R. T. Zahn, S. Honkanen, R. A. Norwood, N. Peyghambarian, K. Kieu, H. Lipsanen, J. Riikonen, *Sci. Rep.* **2015**, *5*, 10334.

[20] C. Janisch, Y. Wang, D. Ma, N. Mehta, A. L. Elías, N. Perea-López, M. Terrones, V. Crespi, Z. Liu, *Sci. Rep.* **2014**, *4*, 5530.

[21] a) I. Shoji, H. Nakamura, K. Ohdaira, T. Kondo, R. Ito, T. Okamoto, K. Tatsuki, S. Kubota, *J. Opt. Soc. Am. B* **1999**, *16*, 620; b) R. G. dos Santos, L. J. Q. Maia, C. B. de Araújo, L. de S. Menezes, *Chin. Opt. Lett.* **2018**, *16*, 041902.

[22] Y. Li, Y. Rao, K. F. Mak, Y. You, S. Wang, C. R. Dean, T. F. Heinz, *Nano Lett.* **2013**, *13*, 3329.

[23] a) C. Couteau, *Contemp. Phys.* **2018**, *59*, 291; b) G. Marino, A. S. Solntsev, L. Xu, V. F. Gili, L. Carletti, A. N. Poddubny, M. Rahmani, D. A. Smirnova, H. Chen, A. Lemaître, G. Zhang, A. V. Zayats, C. De Angelis, G. Leo, A. A. Sukhorukov, D. N. Neshev, *Optica* **2019**, *6*, 1416.

[24] a) J. A. Armstrong, *Appl. Phys. Lett.* **1967**, *10*, 16; b) Y. Kida, Y. Nakano, K. Motoyoshi, T. Imasaka, *Opt. Lett.* **2014**, *39*, 3006.